Engineering Structures 313 (2024) 118292

Contents lists available at ScienceDirect

Engineering Structures

journal homepage: www.elsevier.com/locate/engstruct

Full-scale shaking table tests of cross-laminated timber structures adopting dissipative angle brackets and hold-downs with soft-steel and rubber

Jiawei Chen [a], Zhe Wu [b], Yingda Zheng [b], Tomoki Furuta [c], Haibei Xiong [b,*]

[a] College of Civil Engineering, Nanjing Forestry University, Nanjing, China
[b] College of Civil Engineering, Tongji University, Shanghai, China
[c] Department of Architecture, Nishinippon Institute of Technology, Kitakyushu, Japan

ARTICLE INFO

Keywords:
Cross-laminated timber (CLT)
Novel dissipative connection
Seismic performance
Shaking table test
Numerical simulation

ABSTRACT

Cross-laminated timber (CLT) has recently attracted significant interest in building timber or hybrid structures owing to the rapidly growing demand for low-carbon construction materials with excellent mechanical properties. To investigate the seismic performance of CLT structures adopting novel dissipative angle brackets and hold-downs with soft-steel and rubber (i.e., SRD-ABs and SRD-HDs), a series of shaking table tests were performed on two full-scale specimens, i.e., a benchmark specimen (Specimen I) and a specimen with a multi-doorway at the ground (Specimen II). Several representative ground motions, including the Turkey wave, El Centro wave, Wenchuan wave, and Shanghai artificial wave, were selected as excitations, whose peak acceleration increased gradually from 0.035 g to 0.80 g. The damage patterns of the structures were revealed, and the dynamic characteristics and responses were obtained and analyzed. The results show that the fundamental frequencies of Specimen I and Specimen II were 4.125 Hz and 3.625 Hz, respectively. The mode shapes of each specimen remained similar before tests with peak ground acceleration (PGA) of 0.51 g, with only a slight decrease of approximately 5 % in the fundamental frequency, indicating that the specimens only suffered minor damage because of the great energy-dissipating capacity of the SRD-ABs and SRD-HDs. After experiencing tests with PGA of 0.80 g, the specimen exhibited a maximum inter-story drift of 1/60 with a structural damping ratio of 13 %, and the damage was mainly exhibited at the SRD-ABs and SRD-HDs, which realized the performance objective of replaceability of dissipative connections and repairability of structures under the 9-degree rare earthquakes. Furthermore, non-linear numerical models were developed to duplicate the dynamic characteristics and responses of the test specimen, and the analytical results from the models show satisfactory agreement with the test results. Overall, the outcomes of this paper can provide valuable references for future research and applications of CLT structures with the SRD-ABs and SRD-HDs.

1. Introduction

The CLT structures have become one of the primary structural systems for residential and office buildings in Europe, America, and other regions in recent years, attracting increasing interest from scholars, designers, and government agencies [1–4]. Many studies have been conducted on CLT structures in the last two decades. According to the results of several quasi-static tests and shaking table tests [5–10], the connection system, especially the metal angle brackets and hold-downs for resisting the horizontal sliding and vertical uplift of the walls, usually controls the strength, stiffness, stability, and structural ductility of the CLT structure, since the CLT panels generally exhibit high strength and stiffness, maintaining elasticity without energy dissipation during earthquakes [11]. However, the conventional metal angle brackets and hold-downs, due to the derivation from light wood-frame structures where the input energy is mainly consumed by the numerous sheathing-to-framing connections (i.e., nails or screws), generally have limited energy dissipation capacity, which results in some improvement aspects for CLT structures with conventional metal connections: (1) Undesirable failure modes, such as steel plate fracture or buckling, CLT splitting, and fastener shear-off or withdrawal, are prone to occur [12, 13], which causes difficulties and high costs in repairing CLT shear walls. (2) The CLT structure's energy-dissipating capacity primarily relies on the yielding from metal connections. The limited energy

* Corresponding author.
E-mail address: xiong204@outlook.com (H. Xiong).

https://doi.org/10.1016/j.engstruct.2024.118292
Received 1 November 2023; Received in revised form 21 May 2024; Accepted 25 May 2024
Available online 3 June 2024

dissipation capacity and ductility of conventional metal connections generally result in unsatisfactory seismic resilience [14,15]. (3) The high-strength characteristic of CLT panels is challenging to fully utilize due to the undesirable failure modes and energy dissipation paths [16, 17]. These issues hinder the full utilization of structural advantages of CLT structures in high-intensity areas.

On the other hand, owing to the advantages of CLT structures, significant interest in using CLT in modular construction has recently emerged globally [18–20], especially for tall buildings. It is one of the most effective approaches to overcome the height limitations of CLT structures by combining single or low-rise CLT structures, as modules, with high-rise concrete or steel structures as composite structures. For example, Xiong and Ventura et al. [21] proposed an innovative high-rise concrete-CLT composite structural system, in which a concrete frame-tube structure with a story height of approximately 10 m is adopted as a main structure and several three-story modular CLT structures are constructed on every concrete slab as substructures. The composite structural system has the potential to expand the applications of CLT structures to around 100 m. However, the seismic effects, amplified by the floor of the concrete main structure, raise higher demands on the seismic performance of the CLT substructures [22].

In order to enhance the failure mechanism and seismic performance of CLT structures, researchers have proposed various solutions, most of which focus on developing innovative wall-to-floor connections (i.e., angle brackets and hold-downs). Scotta et al. [23,24] proposed an "X-bracket" that utilizes metal yielding for energy dissipation, serving as a replacement for conventional metal angle brackets. Wrzesniak et al. [25] replaced conventional metal hold-downs with lead extrusion dampers and confirmed their effectiveness in preventing wall damage. D'Arenzo et al. [26] performed reversed cyclic tests on CLT walls using the TITAN V connectors, resulting in generally ductile failure. Polastri et al. [27] tested an energy-dissipating connector, "X-rad", which is placed at the corners of CLT panels to simultaneously transfer horizontal and vertical forces between the wall panels, floor slabs, or foundations. Hashemi et al. [28] introduced a novel energy-dissipating device that combined sliding friction mechanisms and resetting springs in CLT walls, demonstrating its excellent energy dissipation and self-resetting capability. Kramer et al. [29] drew inspiration from the concept of steel buckling-restrained braces to develop a new type of energy dissipator. However, although a large amount of studies has been conducted, most studies either only evaluate the mechanical properties of the connections on a joint level, or are limited to the lateral behavior of CLT walls on a component level, due to the difficulties of test conditions, expense, etc. Few studies have been conducted on experimental research for a full-scale CLT building with innovative connections on a whole structure level, which may be insufficient to evaluate the seismic performance of CLT structures with dissipative connections, especially on their dynamic properties and responses.

To enhance the failure modes, energy dissipation capacity, and seismic resilience of CLT structures under earthquakes and thereby promote the application of CLT structures in areas of high seismic intensity, as well as in high-rise concrete-CLT hybrid structures [21], Xiong et al. [30–32] proposed novel energy dissipative angle brackets and hold-downs (i.e., SRD-ABs and SRD-HDs), featuring with dual energy dissipation mechanism, i.e., yielding of soft steel and shear deformation of rubber. Experimental studies on the dissipative connection joints have confirmed that the SRD-ABs and SRD-HDs have high ductility and energy dissipation capacity. Results of the lateral resistance tests on CLT shear walls with these connections have verified that the damage to the walls was mainly concentrated in the SRD-ABs and SRD-HDs, avoiding damage to CLT panels and screwed joints, which achieves the design goals of "replaceable connections" and "repairable structures". However, despite the advantages of the SRD-ABs and SRD-HDs being verified at both the connection joint level and the shear wall component level, further research at the overall structural level is required to clarify their performance within the whole CLT structures and to reveal the seismic performance of CLT structures with these dissipative connections.

Therefore, this paper reports the shaking table tests of two full-scale three-story CLT structures with the SRD-ABs and SRD-HDs. Several typical earthquake waves were selected and applied to the 8.415 m structures. The failure patterns of the structures under seismic actions were revealed, and the dynamic properties and seismic responses were analyzed. Furthermore, non-linear finite element models were developed in OpenSees to predict seismic performance. The outcomes of this paper are expected to support more valuable references for evaluating the seismic performance of the whole CLT structure with dissipative connections so as to promote the applications of both the CLT structures and the concrete-CLT hybrid structures in the future.

2. Experimental investigation

2.1. Design of the specimens

The full-scale shaking table tests were performed at Tongji University, in which the shaking table has a plane size of 6 m × 4 m and a maximum load-carrying capacity of 70 tons. Two full-scale specimens were tested, including a benchmark specimen (Specimen I) and a specimen with a multi-doorway at the ground (Specimen II). The story number, height, and plane dimension of the specimens were designed based on two main considerations: (1) in compliance with the Chinese codes for fire protection design [33], timber structures are restricted to a maximum of three stories. (2) the test specimens can serve as typical CLT benchmark models for the research on the seismic performance of concrete-CLT hybrid structures, e.g., the innovative high-rise "Concrete frame-tube and timber boxes hybrid structures" [21]. The Specimen I was designed with 3 stories and a total height of 8.415 m, whose plane dimension was 3750 mm × 5940 mm. The openings of the specimens were realized by assembling the separate wall segments and lintel/-parapet elements, which were connected by laminated veneer lumber (LVL) spline joints with self-tapping screws. After all the tests on Specimen I, four CLT parapet elements under the first-floor windows and 8 attached SRD-ABs in the *Y* axis were removed to form Specimen II, as shown in Fig. 1. The Specimen II was set to reflect the architectural requirements of the first floor, and also served as a case for investigating the dynamic characteristics and seismic performance of CLT structures with different first-floor stiffness. The benchmark specimen was designed with a seismic fortification intensity of 8 degrees, and the corresponding design spectral acceleration was 0.30 g. The soil type was set as type IV. These parameters are in accordance with the Chinese Code for Seismic Design of Buildings [34]. The on-site photo of the specimens is shown in Fig. 2.

2.2. Design of the connections

The specimens were connected to the shaking table by a steel extension frame. The CLT panels were made by Western Hemlock with a total thickness of 105 mm (three layers, 35 mm per layer), which were manufactured by the Ningbo Sino-Canada Low-Carbon Technology Research Institute. Co. Ltd.

The SRD-ABs and SRD-HDs were adopted to connect the walls to the CLT floors and the steel extension frame. These dissipative connections, as shown in Fig. 3, are composed of a steel skeleton and rubber, in which the rubber is tightly bonded to the steel skeleton by specially-made adhesives. As validated by the previous experimental and analytical study [30–32], the working mechanism of the SRD-ABs and SRD-HDs can be described as: (1) when the applied load is small, the connection will remain in the elastic state with a large initial stiffness provided by the steel skeleton. (2) As the load increases, the soft-steel dissipative ribs (the bridging part connecting the front and rear plates) will undergo yielding, followed by the shear deformation of the internal rubber. Both processes will consume considerable energy. (3) Meanwhile, it should be

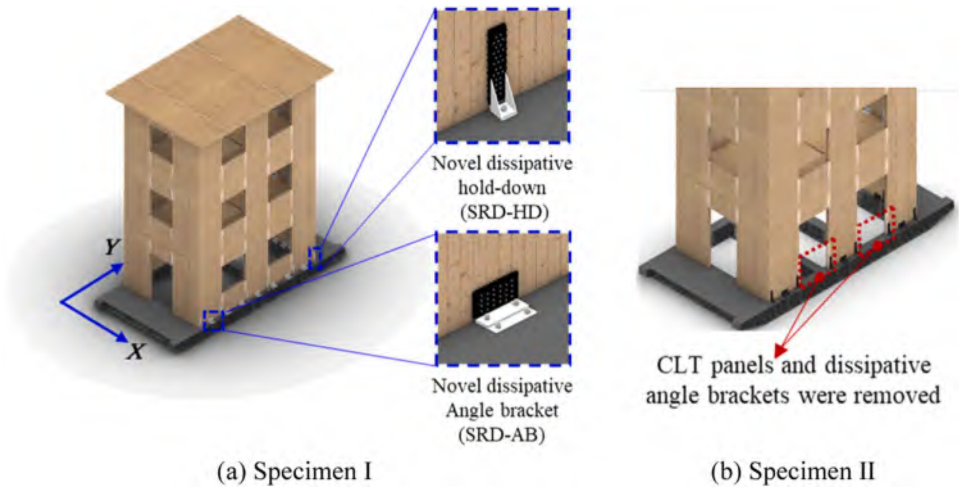

Fig. 1. The test specimens.

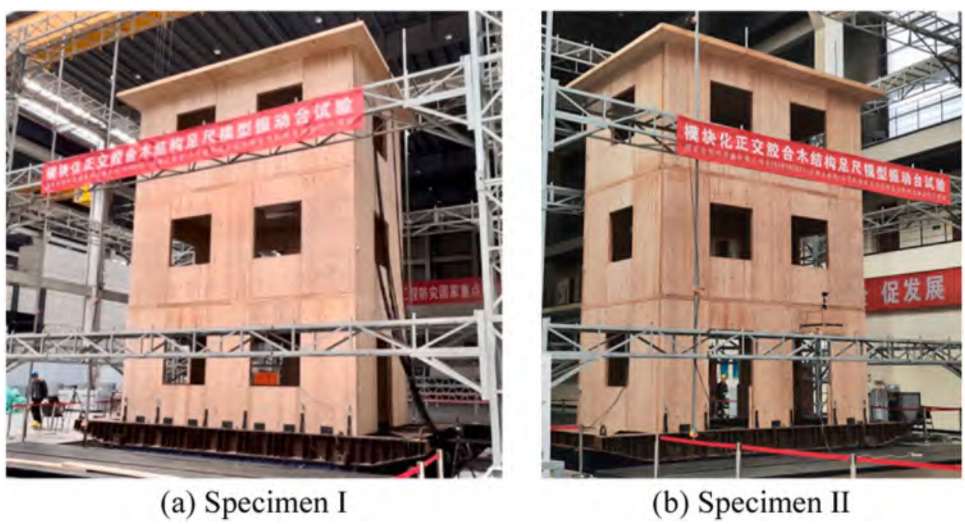

Fig. 2. Photo of the test specimens.

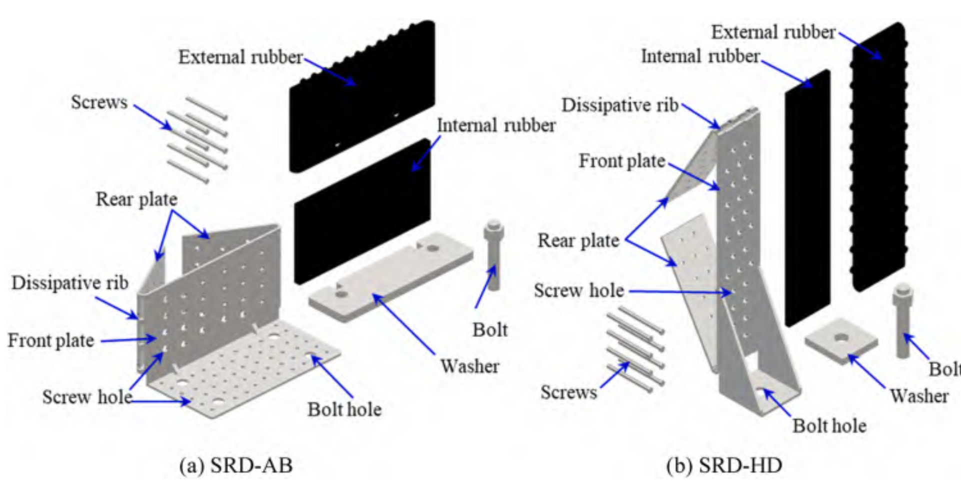

Fig. 3. Diagram of the dissipative connections.

noted that after the fracture of the dissipative ribs, the internal rubber can still be tightly bonded between the front and rear plates, which guarantees the connection can continue to resist the load until the debonding failure of the rubber occurs. Owing to the unique combination of soft steel and rubber, advantages, including high ductility and great energy-dissipating capacity, predictable failure modes and yielding strength, applicability for performance-based designs can be realized [30,32].

As for the tests, the steel skeleton of the SRD-ABs and SRD-HDs was made of 3.5 mm-thick 20# soft-steel, with yielding and ultimate strengths of 245 MPa and 410 MPa, and the elastic modulus and ultimate elongation of 200 GPa and 52.5 %, respectively. The width of the dissipative ribs in the steel skeleton as well as the shear modulus and damping ratio of the rubber were listed in Table 1.

To determine the layout of the SRD-ABs and SRD-HDs on each floor, the seismic load of the structure was calculated and distributed using the equivalent base shear method in Eurocode 8. A similar design process can be referred to in [35]. It should be mentioned that the shear resistance of the SRD-HDs and the tensile resistance of the SRD-ABs were not considered in the calculation. According to the calculation results, the number of SRD-ABs and SRD-HDs on each floor was determined, as shown in Fig. 4.

Self-tapping screws were used to connect adjacent CLT panels of the walls and slabs, as shown in Table 2. For the walls, laminated veneer lumber (LVL) spline joints (using 120 × 35 mm LVL strip) with Φ8.0 mm × 100 mm screws were adopted to connect the in-plane adjacent CLT panels, while Φ8.0 mm × 200 mm screws at 90° were used to connect the CLT panels at transverse direction. As for the slabs, half-lapped joints with Φ8.0 mm × 100 mm screws were used to connect the in-plane panels, while Φ8.0 mm × 200 mm screws were used to fix the slabs to the CLT walls below. It should be noted that the space of the screws was relatively small, while the diameter and length were relatively large. These were determined according to the capacity-based design [36]. In other words, the SRD-ABs and SRD-HDs were designed as dissipative zones, while other connections, including the slab-to-slab screwed joints, slab-to-wall screwed joints, and wall-to-wall screwed joints, were designed as non-dissipative zones and were designed with sufficient over-strength. In these ways, the seismic energy is expected to be consumed by the plastic deformations of the SRD-ABs and SRD-HDs with high ductility and energy-dissipating capacity, whereas other connections can remain elastic. Therefore, the damage will mainly occur at the dissipative connections without damage to the CLT panels or screwed joints. After earthquakes, the structures can be easily repaired by the replacement of the SRD-ABs and SRD-HDs.

2.3. Layout of the sensors

Several types of sensors were adopted to record the acceleration and displacement responses of the specimens. Accelerometers were set at the middle and two corners of each floor, while linear voltage displacement transducers (LVDTs) were set at the diagonal corners to record the absolute acceleration and displacement. Meanwhile, LVDTs were also placed at some adjacent slab panels and between walls and slabs or the foundation to record the relative displacement. The detailed layout of the sensors is shown in Fig. 5.

2.4. Test program

According to the design information, the additional dead and live load were 1.5 kN/m^2 and 2.5 kN/m^2, respectively, while those on the roof were 0.5 kN/m^2. A representative value of gravity load (i.e., 1.0 dead load + 0.5 live load) was used for the seismic analysis. Mass blocks were stuck to floor and roof slabs to represent the additional loads.

Table 1
Parameters of the SRD-ABs and SRD-HDs.

Connection type	Rubber		Dissipative ribs' width (mm)
	Shear modulus (MPa)	Damping ratio	
SRD-ABs	0.4	20 %	9
SRD-HDs	0.4	20 %	10

Several ground motions, including the Turkey wave (February 6, 2023), El Centro wave (May 18, 1940), Wenchuan wave (May 12, 2008), and Shanghai artificial wave #2 (SHW2), were adopted as seismic inputs. Among them, the El Centro wave is a near-earthquake wave with a characteristic period of 0.56 s; the Wenchuan wave belongs to a distant earthquake with a characteristic period of 0.42 s and features a double peak; the Turkey wave is a near-earthquake, having strong destructiveness with a characteristic period of 1.12 s; the SHW2 wave is an artificial earthquake wave based on the fitting of the China seismic design response spectrum, featuring a longer plateau segment with a characteristic period of 0.72 s. Fig. 6 depicts the unscaled spectral accelerations of the selected excitations. To match the provisions of the Chinese codes [34], the peak ground acceleration (PGA) of the selected ground motions was scaled to pre-set values. These values vary from 0.035 g to 0.80 g, which covers minor earthquakes, moderate earthquakes, and rare earthquakes (63 %, 10 %, and 2 % probability of exceedance in 50 years) of intensity 7.0, 8.0, 8.5, and 9.0. Table 3 and Table 4 list the detailed test program. On the other hand, the longitudinal (i.e., Y axis in Fig. 1) direction is the primary direction for the seismic excitation. To consider the impact of bidirectional seismic excitation, excitations in both X and Y directions were simultaneously introduced in some cases. Based on the Chinese codes [34], the PGA ratio should be set as 0.85 between the secondary and primary directions. Meanwhile, it should be mentioned that the specimens were subjected to wideband white noise excitation before and after each seismic excitation to obtain the dynamic characteristics (i.e., frequency, mode shape, and damping ratio).

3. Test results and analysis

3.1. Damage inspection

For Specimen I, after tests under the seismic excitation with PGA of 0.10 g, the seismic response of the specimen was relatively small. No obvious deformations, cracks or pull-out, or shear-off of the screws were observed at the connections or the CLT panels. After the tests with a PGA of 0.22 g, no visible deformation was observed at the connections of the first floor. On the second floor, one screw in a SRD-AB was sheared off, and one screw was slightly pulled out, but the other screws were in good condition without damage. No visible deformation was observed at the connections on the third floor, but some shrinkage cracks extended on some roof and wall panels.

In the subsequent tests, the maximum PGA of the seismic excitation reached 0.62 g, which was in accordance with rare earthquakes of intensity 9.0 in Chinese design codes. Nevertheless, the specimen exhibited controllable deformation and returned to its original position without significant tilting or damage. The external rubber of some SRD-HDs exhibited a tightening phenomenon, as shown in Fig. 7, indicating that the dissipative ribs experienced relative deformation during the tests. No fracture of the dissipative ribs or the debonding of the rubber was observed.

As for Specimen II, it exhibited more significant deformation under seismic excitation due to the removal of the wall panels and the SRD-ABs. However, the specimen still showed excellent deformation recovery capability. During the tests, significant uplifting of the corner walls on the first floor was observed. For example, under the excitation of the El Centro wave with a PGA of 0.80 g, the maximum uplifting distance can approximately reach 1.5 cm, as shown in Fig. 8.

After all the tests with PGA of 0.8 g were completed, it was observed that approximately half of the SRD-HDs and some SRD-ABs on the first floor exhibited significant relative deformation and fracture in the dissipative ribs. Some screws showed noticeable horizontal and vertical shear deformations, especially those at the corner walls. On the second floor, some SRD-ABs suffered damage to the dissipative ribs, but no damage was observed in the SRD-HDs. Meanwhile, some screws were pulled out, both at SRD-ABs and SRD-HDs. As for the third floor, no

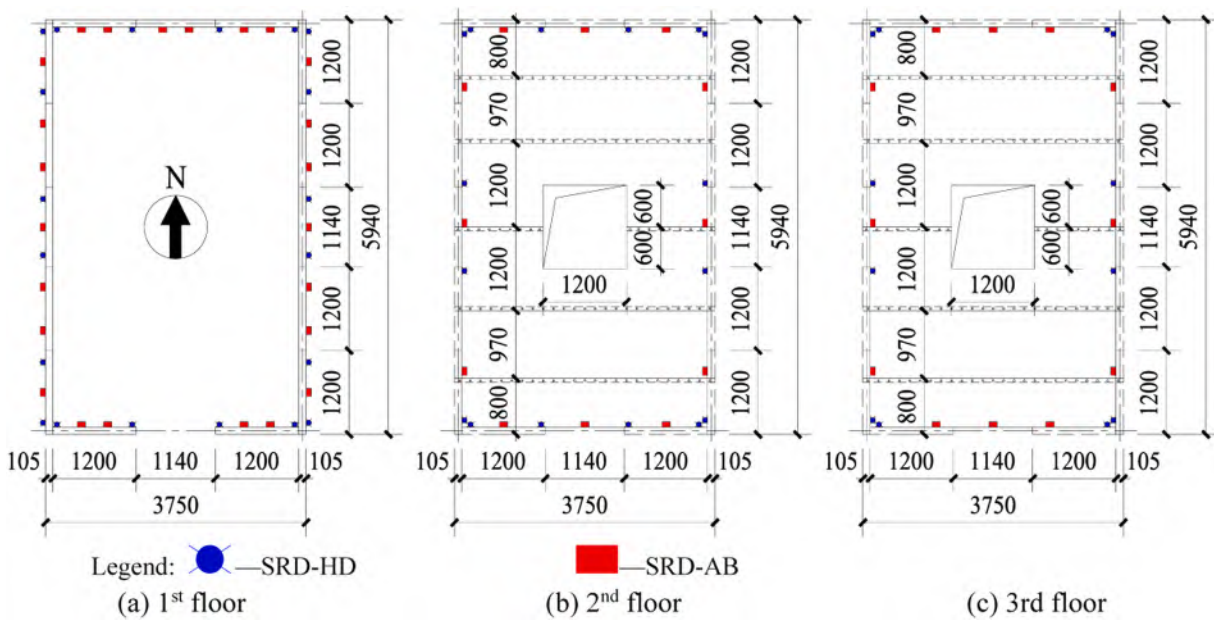

Fig. 4. Layout of the SRD-ABs and SRD-HDs.

Table 2
Layout of the screwed connections.

Connection type	Self-tapping screws (mm)			Note
	Diameter	Length	Space	
Wall-to-wall in-plane connection	8.0	100	100	LVL spline joints
Wall-to-wall connection in transverse direction	8.0	200	150	
Slab-to-slab in-plane connection	8.0	100	150	Half-lapped joints
Slab-to-wall connection	8.0	200	150	

relative deformation was found in the dissipative connections. It should be mentioned that no visible damage was observed at the screwed connections and the CLT panels. The typical failure phenomenon is shown in Fig. 9.

3.2. Dynamic identification

During the tests, white noise excitations were performed to identify the dynamic characteristics of the specimens. Table 5 lists the changes in natural frequencies and damping ratios of the specimens under different excitation conditions. It can be seen that for Specimen I, the first three modes are translational motions in the X and Y directions and torsion,

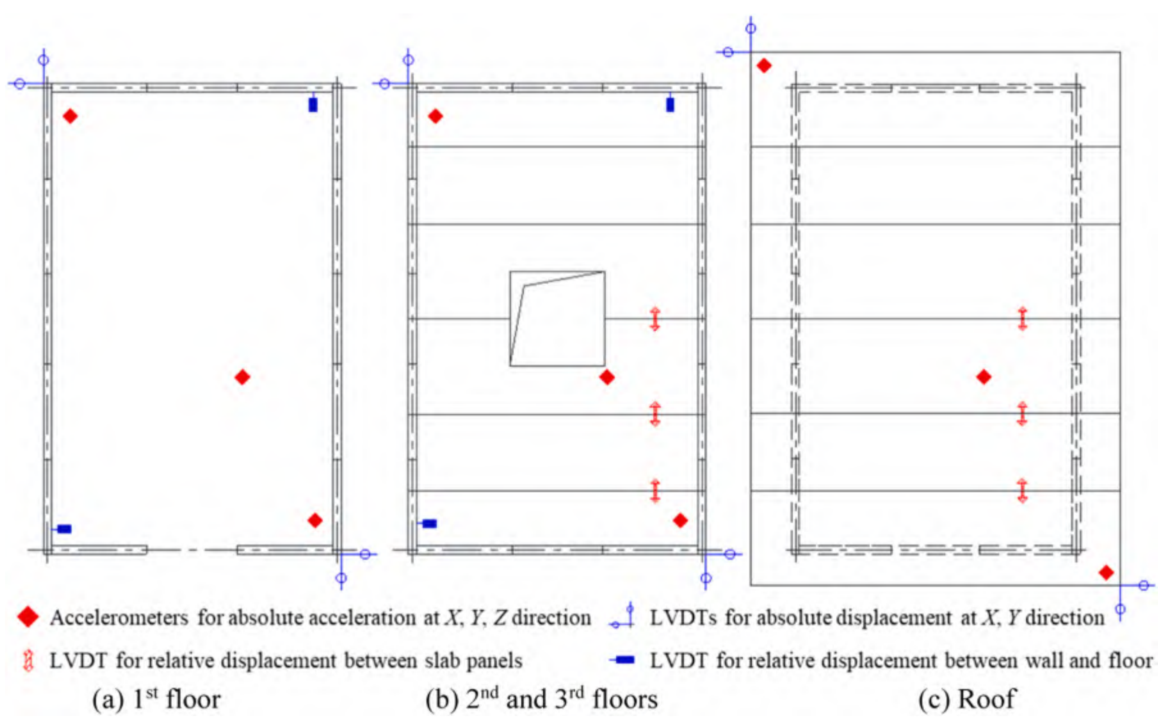

Fig. 5. Layout of the sensors.

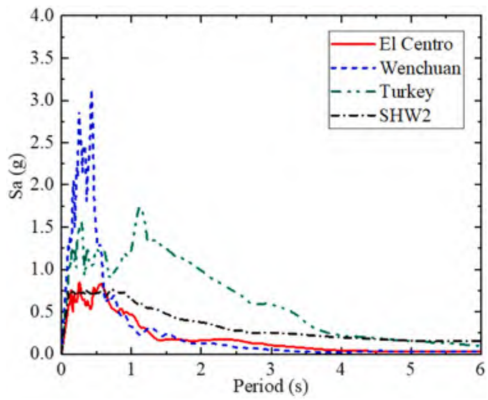

Fig. 6. Unscaled spectrum of the selected ground motions.

indicating that the lateral stiffness of the specimen in the *Y* direction is greater than that in the *X* direction. After the tests with a PGA of 0.40 g, the specimen showed a decreasing trend in the natural frequency, with a decrease of approximately 5 %, indicating a decrease in stiffness.

Under the progressive excitations in the *Y* direction, damage accumulated in the *Y*-axis components, causing a decrease in the frequency. Additionally, due to the removal of the wall panels and SRD-ABs in Specimen II, its first three modes changed to translational motions in the *Y* and *X* directions and torsion.

It is worth noting that the *Y*-axis translational frequency of Specimen II decreased by 29.27 %, and the torsional frequency decreased by 15.87 % compared with Specimen I. The main reasons can be attributed to the fact that the model modification involves reducing and removing wall panels and connections, as well as the potential damage at the screwed joints connecting the CLT panels due to the cumulative damage after multiple tests. On the other hand, the fundamental frequency of the specimen decreased with increasing seismic intensity. However, there was no significant decrease in the frequency before the tests under excitation with PGA of 0.51 g (i.e., corresponding to the rare earthquake of 8.5 degrees), indicating that the structure was in the elastic stage or only had minor damage, which verifies that the SRD-ABs and SRD-HDs have satisfactory performance for consuming energy and mitigating response for the CLT structures.

On the other hand, generally, the damping ratio of the specimens increased as the seismic intensity increased due to the damage accumulation at the SRD-ABs and SRD-HDs. For Specimen I, its damping ratio increased from 3 % to 5 %, while that of Specimen II increased from 10 % to 13 % in the *Y* direction and remained around 7 % in the *X* direction when all the tests were completed.

Fig. 10 depicts the changes in translational mode shapes of the specimens during the incremental excitation process, in which the axis number '1' refers to the top of the walls on the first floor while others are similar. It can be seen that for Specimen I, its mode shape under different seismic excitations was similar, indicating slight structural damage. However, for Specimen II, especially in the *X* direction, there was a noticeable change in the translational mode shapes after the seismic excitations with PGA of 0.62 g, indicating that significant damage has

Table 3
Test program of Specimen I.

No.	Record	PGA (g)		Note	No.	Record	PGA (g)		Note
		X	*Y*				*X*	*Y*	
1	White noise	0.07	0.07		15	El Centro		0.40	Rare
2	El Centro		0.0035	Minor	16	Wenchuan		0.40	earthquake
3	Wenchuan		0.0035	earthquake	17	Wenchuan	0.34	0.40	of intensity 8.0
4	SHW2		0.0035	of intensity 7.0	18	SHW2		0.40	
5	White noise	0.07	0.07		19	White noise	0.07	0.07	
6	El Centro		0.10	Moderate	20	El Centro		0.51	Rare
7	Wenchuan		0.10	earthquake	21	Wenchuan		0.51	earthquake
8	SHW2		0.10	of intensity 7.0	22	Wenchuan	0.434	0.51	of intensity 8.5
9	White noise	0.07	0.07		23	SHW2		0.51	
10	El Centro		0.22	Rare	24	White noise	0.07	0.07	
11	Wenchuan		0.22	earthquake	25	El Centro		0.62	Rare
12	Wenchuan	0.187	0.22	of intensity 7.0	26	Wenchuan		0.62	earthquake
13	SHW2		0.22		27	Wenchuan	0.527	0.62	of intensity 9.0
14	White noise	0.07	0.07		28	SHW2		0.62	
					29	White noise	0.07	0.07	

Table 4
Test program of Specimen II.

No.	Record	PGA (g)		Note	No.	Record	PGA (g)		Note
		X	*Y*				*X*	*Y*	
1	White noise	0.07	0.07		15	Wenchuan		0.51	Rare
2	El Centro		0.22	Rare	16	Wenchuan	0.434	0.51	earthquake
3	Wenchuan		0.22	earthquake	17	SHW2		0.51	of intensity 8.5
4	Wenchuan	0.187	0.22	of intensity 7.0	18	Turkey		0.51	
5	SHW2		0.22		19	White noise	0.07	0.07	
6	Turkey		0.22		20	El Centro		0.62	Rare
7	White noise	0.07	0.07		21	Wenchuan		0.62	earthquake
8	El Centro		0.40	Rare	22	Wenchuan	0.527	0.62	of intensity 9.0
9	Wenchuan		0.40	earthquake	23	SHW2		0.62	
10	Wenchuan	0.34	0.40	of intensity 8.0	24	White noise	0.07	0.07	
11	SHW2		0.40		25	El Centro		0.80	
12	Turkey		0.40		26	Wenchuan		0.80	
13	White noise	0.07	0.07		27	White noise	0.07	0.07	
14	El Centro		0.51						

Note: Due to the deformation limitation of the shaking table, tests with SHW2 (PGA of 0.80 g) and Turkey (PGA of 0.62 g and 0.80 g) waves were not performed.

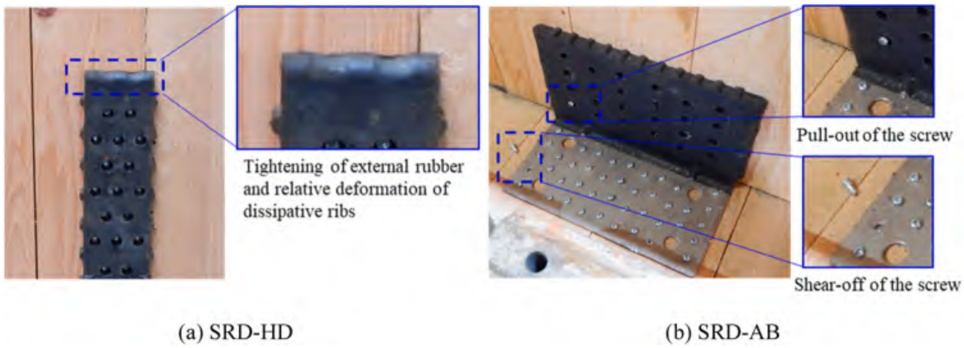

Fig. 7. Phenomenon of the dissipative connections in Specimen I.

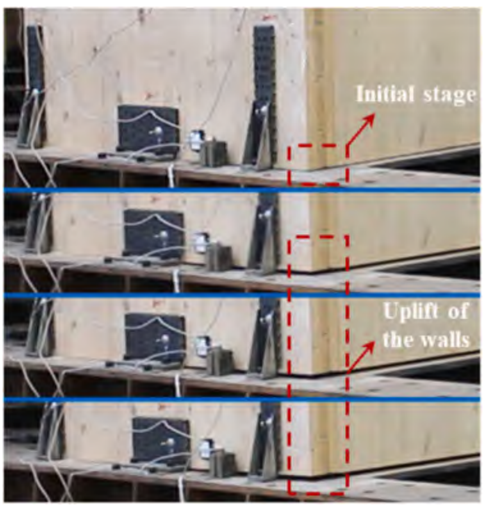

Fig. 8. Significant uplifting at the bottom walls during the tests in Specimen II.

occurred. This is consistent with changes in the natural frequencies. Meanwhile, as can be observed from the second-order translational mode shape curves, both specimens had peak mode shape coefficients on the roof, and the coefficient values of the roof were much larger than those of the second floor, which indicates a pronounced whip effect on the roof.

3.3. Acceleration response

The change patterns of maximum floor acceleration response in the X and Y directions under different seismic excitations are similar. Fig. 11 and Fig. 12 show the floor acceleration amplification factors α (i.e., the ratio between the peak floor acceleration and the peak ground acceleration) under different seismic excitations for Specimen I and Specimen II, respectively, while Fig. 13 shows the variation of average factors of different floors. It can be seen that: (1) The distribution of the α factors generally follows an inverted triangle shape from the bottom up. In other words, the floor accelerations increase as the height increases. However, for Specimen II, due to the decrease of the lateral stiffness, there is an obvious increase in the first-floor acceleration response, resulting in close values for the first-floor and second-floor α factors. Additionally, the first-floor α factors of Specimen II are also larger than those of Specimen I. (2) The average value of the α factors ranges from 1.3 to 4.2 for Specimen I, while that ranges from 1.2 to 2.8 for Specimen II. Except for the first floor, the Specimen I has significantly higher α factors than Specimen II. It can be attributed that Specimen II had more significant damage that caused a rapid increase in the structural damping ratio, which effectively mitigated the acceleration responses. (3) The α factors of Specimen I decrease significantly with increasing PGA of excitations, but the decreasing trend gradually slows down. This is because of the increasing damping ratio caused by the gradual damage

Table 5
Frequencies and damping ratios of the specimens under different excitations.

Specimen	Excitation case	Natural vibration frequency (Hz)			Damping ratio	
		X	Y	Rotation	X	Y
Specimen I	Initial	4.125	5.125	7.875	0.030	0.037
	0.035 g	4.125	5.000	7.875	0.030	0.038
	0.10 g	4.125	5.000	7.875	0.030	0.038
	0.22 g	4.125	4.875	7.750	0.045	0.051
	0.40 g	4.000	4.875	7.750	0.047	0.051
	0.51 g	3.875	4.750	7.500	0.048	0.053
	0.62 g	3.875	4.625	7.500	0.048	0.053
Specimen II	Initial	3.750	3.625	6.625	0.067	0.100
	0.22 g	3.750	3.625	6.625	0.067	0.103
	0.40 g	3.750	3.500	6.625	0.067	0.103
	0.51 g	3.750	3.375	6.625	0.067	0.111
	0.62 g	3.625	3.000	6.375	0.069	0.125
	0.80 g	3.625	3.000	6.250	0.069	0.130

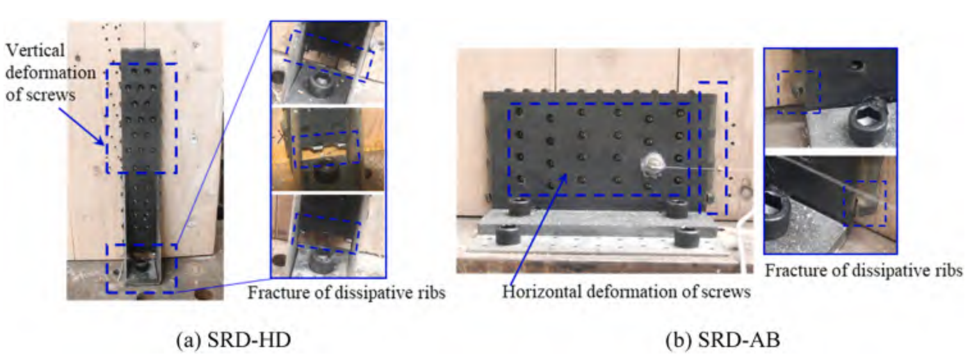

Fig. 9. Phenomenon of the dissipative connections in Specimen II.

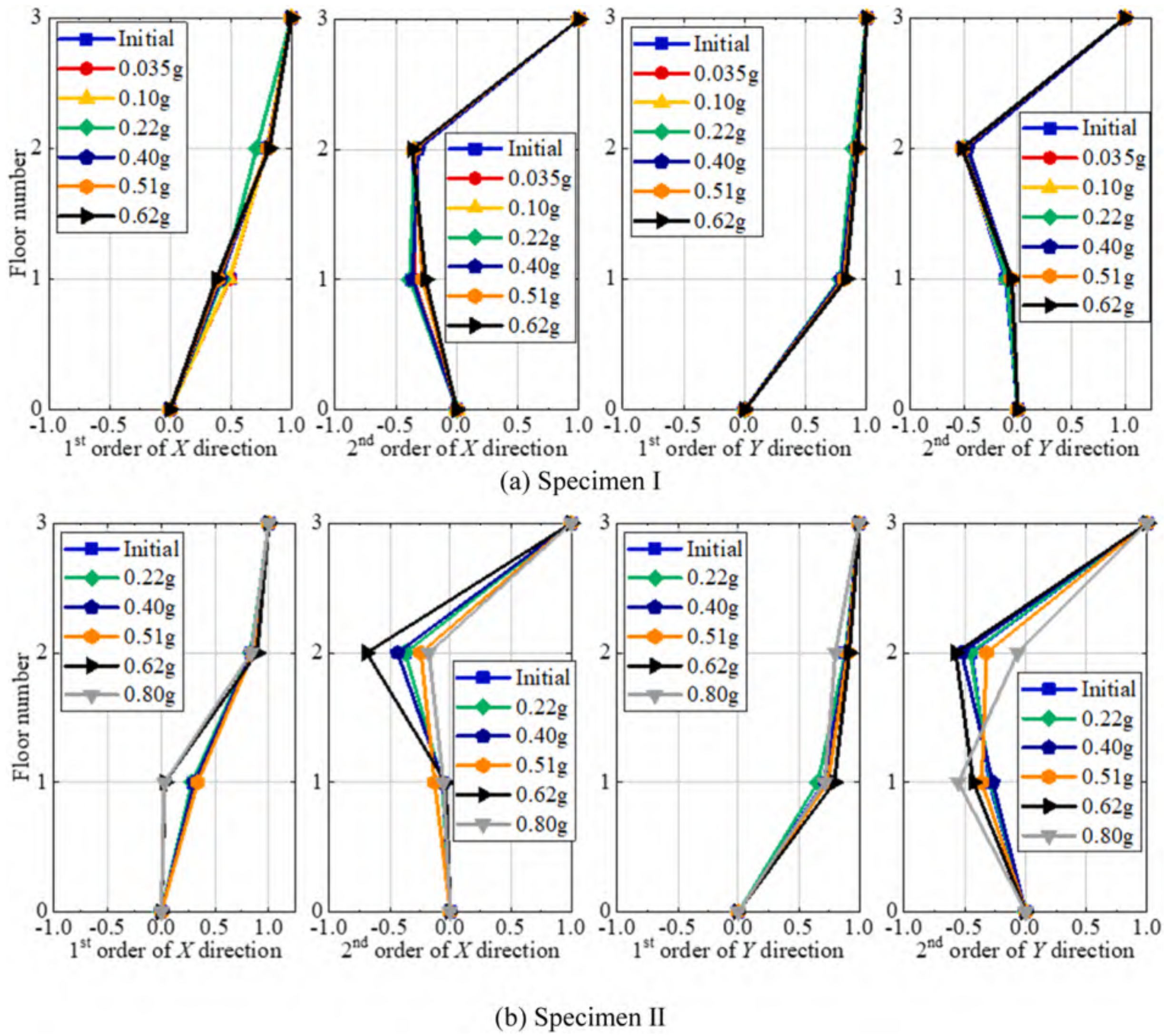

Fig. 10. Translational mode shapes of the specimens.

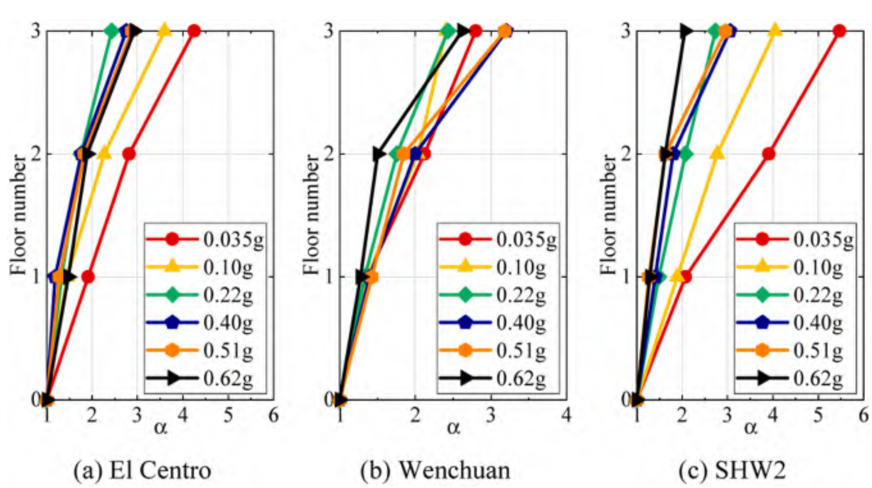

Fig. 11. Acceleration amplification factors α of Specimen I.

as the earthquake intensity increased. However, for Specimen II, its α factors gradually increase with enhanced PGA of excitations. The reason is that the increment in damping ratio was relatively small, while the decrease in stiffness led to a significant increase in the structure period, which was closer to the characteristic period of the excitations and thus resulted in increased acceleration response. Overall, the floor

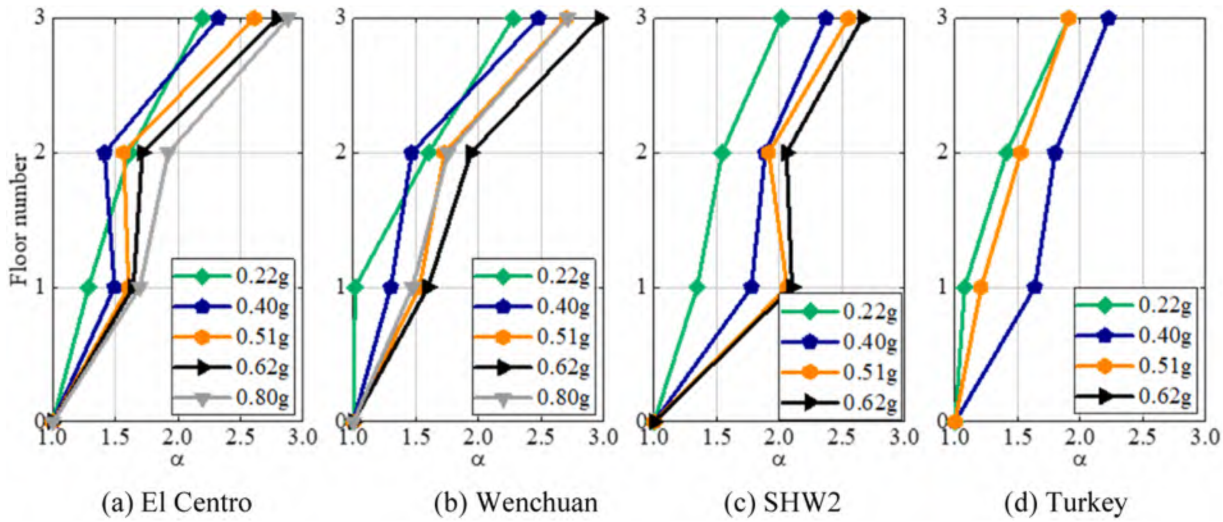

Fig. 12. Acceleration amplification factors α of Specimen II.

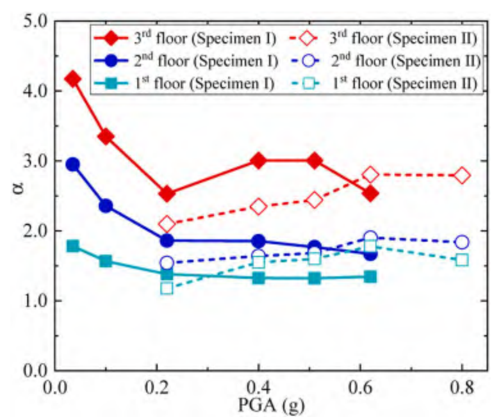

Fig. 13. Variation of average α factors.

acceleration amplification coefficient of the specimens is related to the structure's period and damping ratio and spectrum characteristics of the seismic waves.

3.4. Displacement response

The maximum inter-story displacement under different excitations occurred on the first floor of the specimens. Fig. 14 depicts the maximum inter-story drift as well as displacement in the *Y*-axis of the specimens. It can be observed that: (1) Due to the relatively lower first-floor stiffness, the maximum inter-story drift of Specimen II is obviously larger than that of Specimen I. (2) For both Specimen I and Specimen II, they were in the elastic stage or only suffered slight damage during the excitations with PGA lower than 0.51 g. Thus, their natural frequency did not show a significant decrease, and the inter-story displacement of the first floor was approximately linearly correlated to the earthquake intensity. (3) As the specimens' damage gradually accumulated, their stiffness and natural frequency decreased. Therefore, under the identical increment of the seismic intensity, the inter-story displacement of the first floor increased significantly.

It is worth noting that, even for Specimen II, where several CLT wall panels were removed on the first floor, its maximum inter-story drift was 1/60 during the tests with a PGA of 0.80 g. The evaluation of the maximum inter-story drift from a safety and reliability perspective indicates that the CLT structures with SRD-ABs and SRD-HDs show excellent seismic resilience, and their seismic performance can be regained by replacing the damaged dissipative connections, even after rare earthquakes.

3.5. Shear-weight ratio

The shear-weight ratio (i.e., the ratio of floor shear force to the total

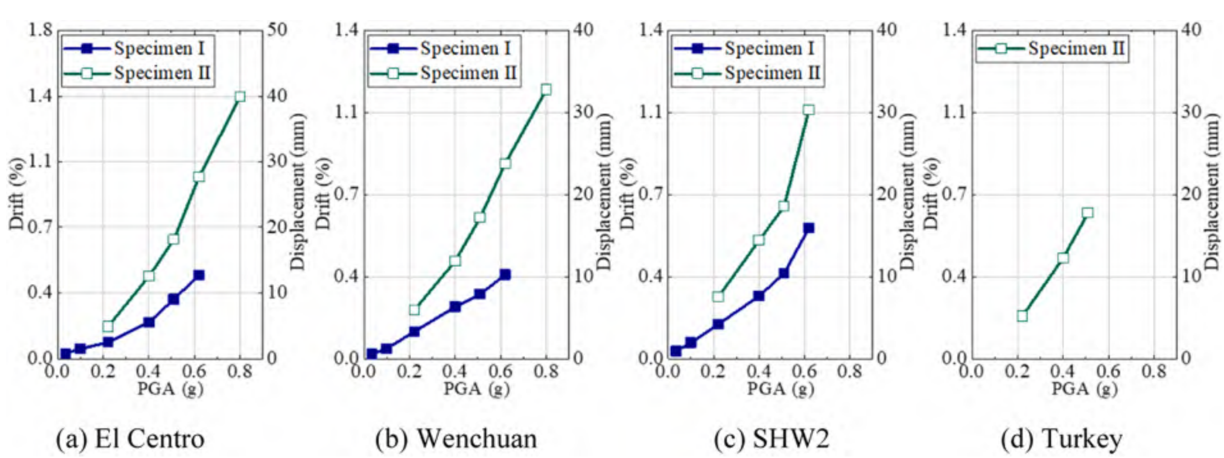

Fig. 14. The maximum inter-story drift and displacement in the *Y*-axis.

weight of the structure) is a widely used parameter for evaluating the shear force in the structural design. Fig. 15 and Fig. 16 show the floor shear forces under different seismic intensities. The shear-weight ratio gradually increases as the seismic intensity increases. Meanwhile, with the increase of the building height, the floor shear force approximately linearly decreases. These can be attributed to the relationship between the seismic action and the product of the floor acceleration amplification factor and the floor mass ratio. As shown in Table 6, this relationship can be summarized as that the seismic action of each floor (i.e., E_i) divided by the base shear (i.e., the total seismic action of each floor ΣE_i) is approximately equal to the product of the mean floor acceleration amplification factor α_i and the floor mass ratio β_i (i.e., $S_i = \alpha_i \times \beta_i$) divided by the sum of the product of each floor (i.e., ΣS_i), as shown in Eq. (1). Such relationship provides a valuable reference for future design.

$$\frac{E_i}{\sum E_i} \approx \frac{S_i}{\sum S_i} = \frac{\alpha_i \beta_i}{\sum \alpha_i \beta_i} \tag{1}$$

3.6. Capacity spectrum curve

The capacity spectrum curve of a structure refers to the spectral acceleration-displacement relationship of the equivalent single-degree-of-freedom system derived from the pushover curve, which is widely used for evaluating seismic performance [37]. In this paper, the capacity spectrum curves were plotted by the relationship between the base shear-weight ratio and the roof displacement, in which the base shear was calculated from the floor mass and acceleration and the displacement was recorded by the LVDTs. The slope of the curve represents the overall lateral stiffness of the structure, which can reflect changes in the lateral performance.

Fig. 17 depicts the distribution of the test data points of Specimen I under different excitations. The capacity spectrum curves were obtained by fitting logarithmic curves to the data. It can be seen that the shapes of the capacity spectrum curves under the excitation of different seismic waves are similar. The structure's general lateral stiffness decreases slightly as the roof displacement increases, which is due to the accumulation of structural damage.

Fig. 18 compares the capacity spectrum curves of Specimen I and Specimen II. The shapes of the capacity spectrum curves under different seismic waves are similar. According to the changing trend of the tangent slope, the overall lateral stiffness of Specimen I is higher than that of Specimen II, but the curve shape generally maintains an approximate linear relationship, indicating that most of the structural deformation is elastic deformation. The lateral stiffness of Specimen II decreased significantly due to the removal of the CLT wall panels and connections. Nevertheless, the specimen still maintained great elastic deformation capacity even under the excitations with a PGA of 0.80 g. The maximum roof displacement was close to 100 mm, and the base shear-weight ratio was about 1.80, which indicates that the CLT structures with SRD-ABs and SRD-HDs have excellent seismic performance thanks to the great load-carrying capability, ductility and energy-dissipation capacities of the dissipative connections.

4. Numerical simulation

The open-source software package Open System for Earthquake Engineering Simulation (OpenSees) version 2.5.0 was adopted to simulate the tested specimen I. For the CLT panels, shellMITC4 element with elastic orthotropic material was adopted since no damage was observed. The Shear Analogy Method [38] was adopted to determine the equivalent moduli of elasticity in the X and Y directions, which was obtained as 1020 MPa and 14800 MPa, respectively. Meanwhile, the Zero-length element was adopted to model the compressive contact between the wall bottom and the slab or foundation, combined with the elastic-no-tension (ENT) material model.

For the simulation of SRD-ABs and SRD-HDs, the Zerolength element with the Pinching4 material model was adopted. The Pinching4 material models for the shear or tension properties were calibrated by the connection test results, as shown in Fig. 19. For the SRD-ABs, both the shear and tension properties were considered, while only the tension properties were considered for the SRD-HDs since their shear properties are weak. The SRD-HDs connecting the wall panel to the steel foundation (i.e., WG-HD-T) or the CLT floor (i.e., WF-HD-T) were tested to obtain their tension properties. The tension properties of the SRD-ABs connecting the CLT wall panel to the foundation (i.e., WG-AB-T) or the CLT floor (i.e., WF-AB-T), as well as their shear properties (i.e., WG-AB-S or WF-AB-S) were also tested in the previous study, as shown in Fig. 19. As for the screwed joints, the Zerolength element with Pinching4 material model was used to simulate the tension and shear properties. The test results in reference [39] were adopted for the calibration of the Pinching4 material models. Fig. 20 shows the final finite element (FE)

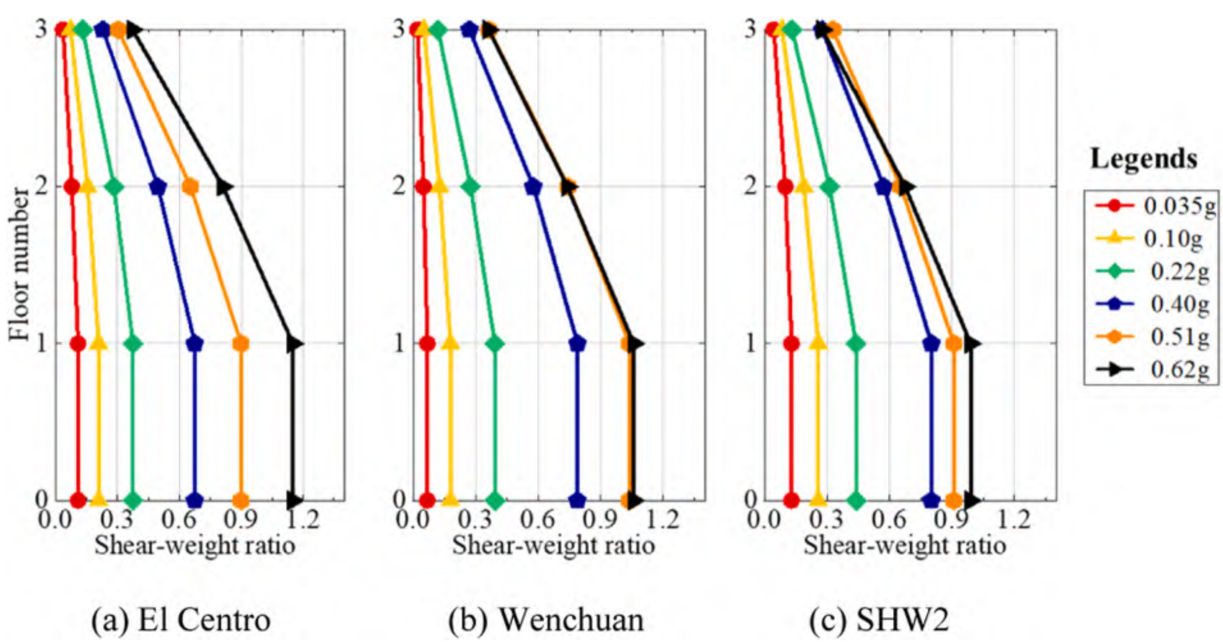

Fig. 15. Floor shear in the Y-axis of Specimen I.

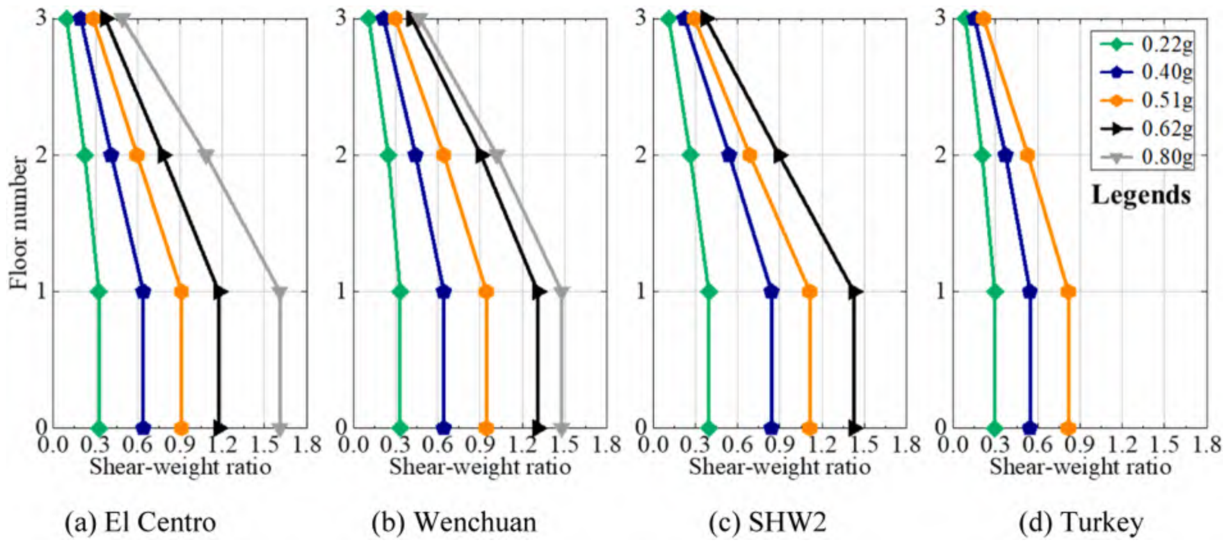

Fig. 16. Floor shear in the Y-axis of Specimen II.

Table 6
Relation between the seismic action and product of the α and β factors.

Specimen	Floor number	Mean acceleration amplification factor α_i	Floor mass ratio β_i	$S_i = \alpha_i \times \beta_i$	S_i / ΣS_i	Seismic action / Base shear	Error
Specimen I	1	1.45	39.1 %	0.57	27.68 %	28 %	1.15 %
	2	2.08	39.3 %	0.82	39.73 %	39 %	1.88 %
	3	3.10	21.6 %	0.67	32.59 %	33 %	1.25 %
Specimen II	1	1.54	39.1 %	0.60	33.10 %	33 %	0.31 %
	2	1.72	39.3 %	0.68	37.22 %	39 %	4.57 %
	3	2.50	21.6 %	0.54	29.68 %	29 %	2.35 %

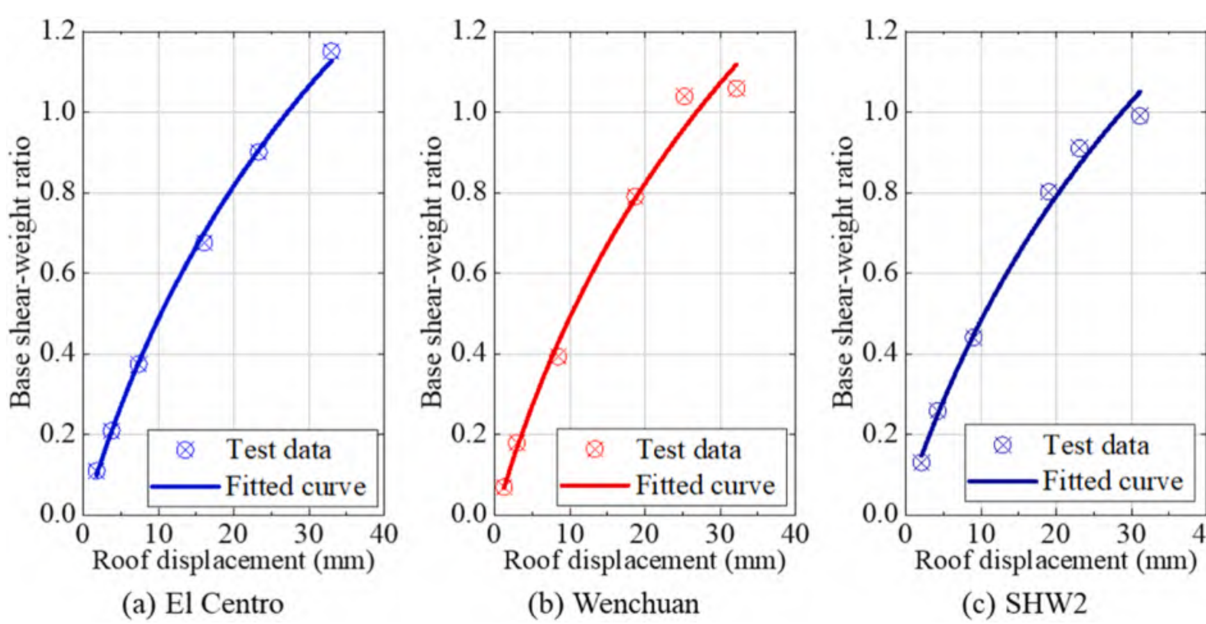

Fig. 17. Capacity spectrum curve of Specimen I.

model, which is depicted by the NextFEM Designer post-processing software.

To verify the accuracy of the FE model, the dynamic properties and the seismic responses of the FE model and the tested specimen were compared. Table 7 lists the values of the first six natural frequencies and vibration modes, while Fig. 21 shows the first three vibration modes. It can be seen that the natural frequencies and vibration modes of the tested specimen and FE model are in good agreement, which indicates that the FE model can reasonably predict the basic dynamic properties.

Table 8 and Fig. 22 illustrate the floor acceleration responses of the tested specimen and FE model under the excitation of El Centro, Wenchuan, and SHW2 waves with PGA of 0.10 g, 0.22 g, and 0.40 g, respectively. The results of the FE model offer satisfactory agreement with test results in terms of tendency and peak values of the time-history

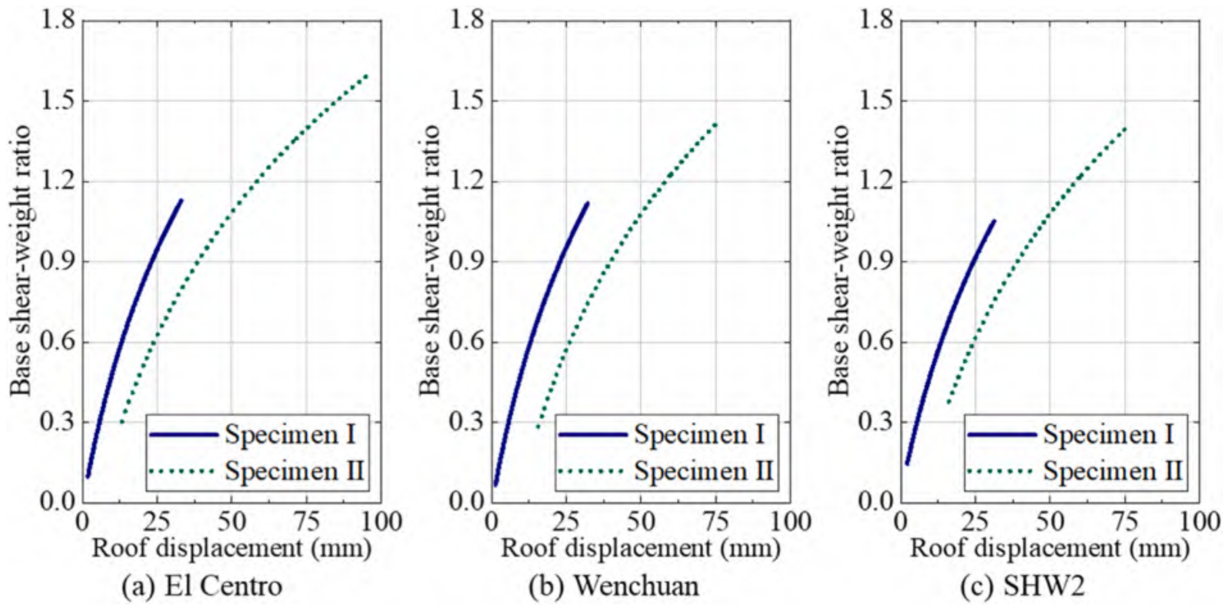

Fig. 18. Comparison of capacity spectrum curves of Specimen I and II.

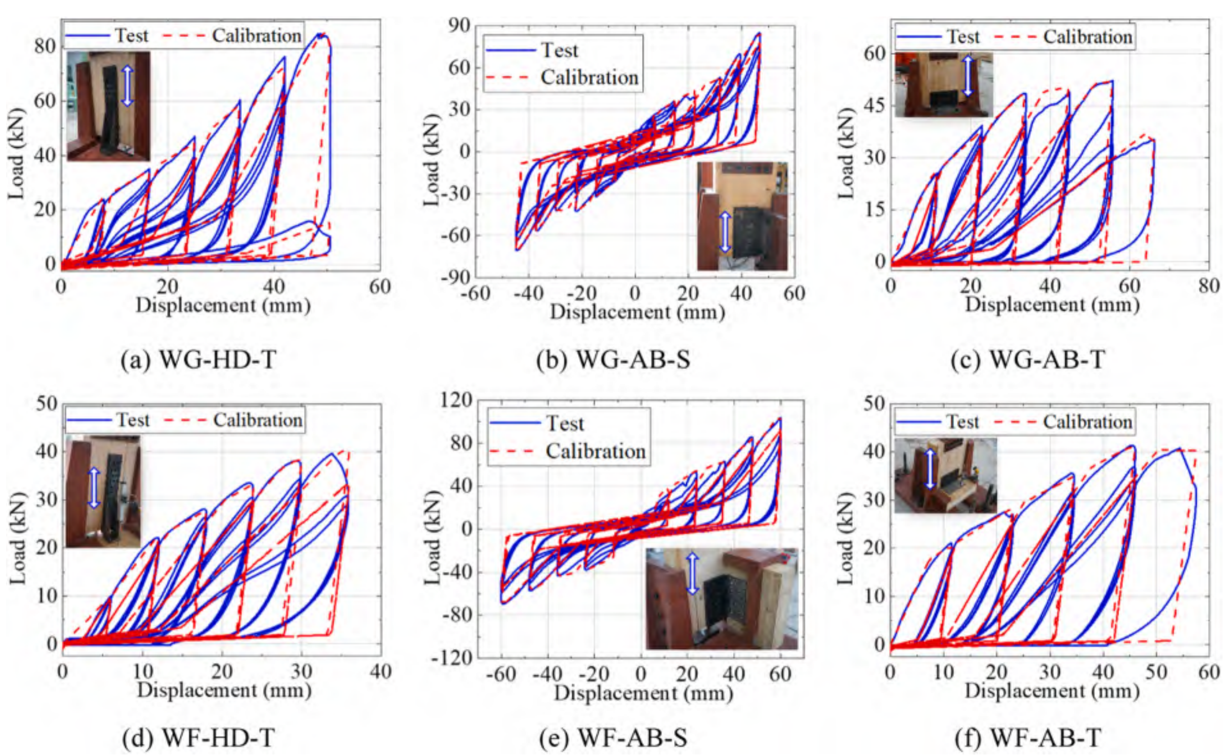

Fig. 19. Comparison of test results and calibration of the SRD-ABs and SRD-HDs.

curves, although differentials can be observed. Nevertheless, the average estimation error of the peak acceleration of each floor is in the range of 5.8 % to 8.6 %, indicating satisfactory accuracy of the developed FE model for estimating the floor acceleration responses.

Table 9 compares the inter-story displacement between the tested specimen and the FE model. The estimated error ranges from 5.8 % to 24.1 %, and the average error varies from 12 % to 16 %, which is satisfactory for engineering practice.

Overall, the comparison of dynamic properties and seismic responses between the tested specimen and the FE model validates the effectiveness of the numerical model, which can serve as a tool for future parameterized analyses for CLT structures with novel dissipative connections.

5. Discussion

To further compare the seismic behavior of CLT structures with either dissipative connections or conventional metal connections, numerical analysis was performed based on the finite element models established previously. Specifically, the calibrated parameters for the material models of the SRD-ABs and SRD-HDs were replaced with those of conventional metal connections, as provided by reference [40].

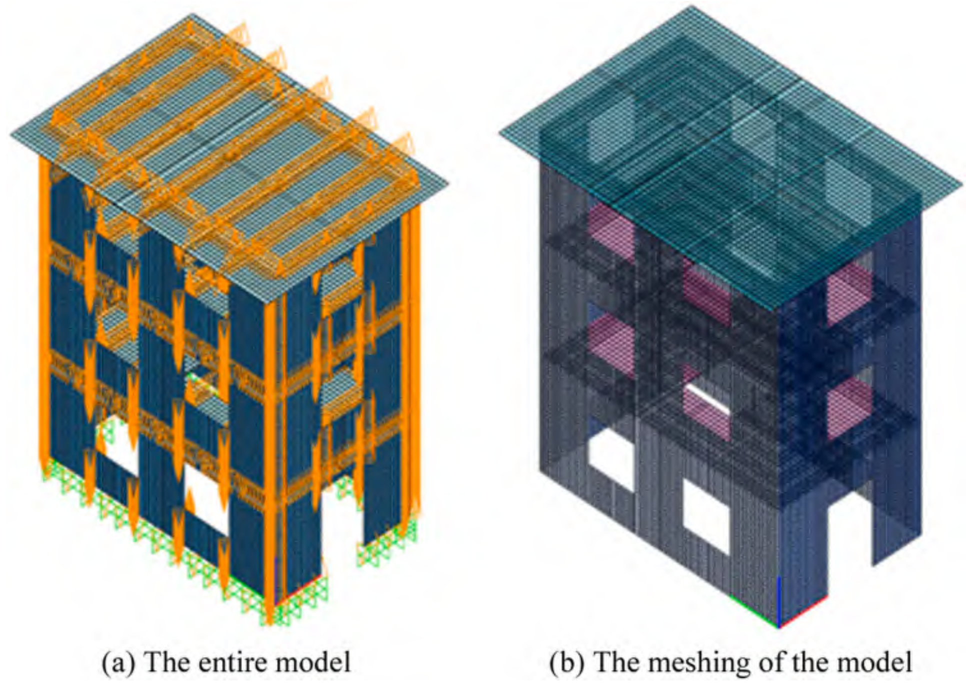

Fig. 20. The finite element model developed in OpenSees.

Table 7
Comparison of natural frequencies.

No.	Natural frequency (Hz)			Vibration mode
	Tested specimen	FE model	Error	
1st mode	4.125	4.167	0.98 %	Translational mode in *X* direction
2nd mode	5.125	5.090	0.68 %	Translational mode in *Y* direction
3rd mode	7.875	7.142	9.31 %	Torsional mode
4th mode	10.880	10.876	0.04 %	Translational mode in *X* direction
5th mode	14.380	13.855	3.65 %	Translational mode in *Y* direction
6th mode	15.880	16.084	1.28 %	Translational mode in *X* direction

Non-linear time-history analysis was performed on the two FE models under excitation of the Wenchuan wave with a PGA of 0.80 g. The analysis results indicate that: (1) In terms of energy dissipation capacity, as shown in Fig. 23, the total cumulative hysteretic energy dissipation E_d

Table 8
Comparison of peak floor acceleration.

Excitation	Floor number	Peak acceleration (m/s^2)			
		Tested specimen	FE model	Error	Average error
El Centro	1	1.29	1.42	9.37 %	8.62 %
	2	2.05	1.87	8.61 %	
	3	3.24	2.98	7.87 %	
Wenchuan	1	2.84	2.54	10.66 %	7.99 %
	2	3.87	4.18	8.11 %	
	3	5.33	5.61	5.21 %	
SHW2	1	5.56	5.78	4.02 %	5.81 %
	2	7.25	8.05	10.98 %	
	3	12.37	12.07	2.43 %	

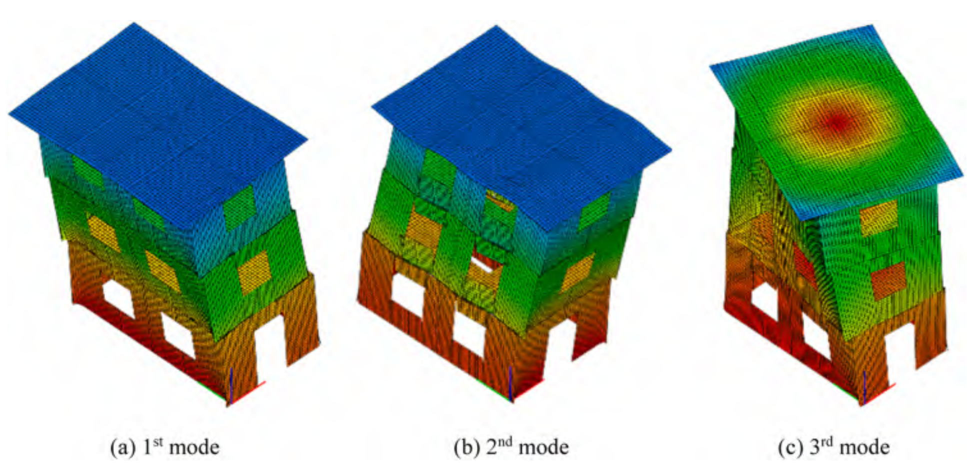

Fig. 21. First three vibration modes of the finite element model.

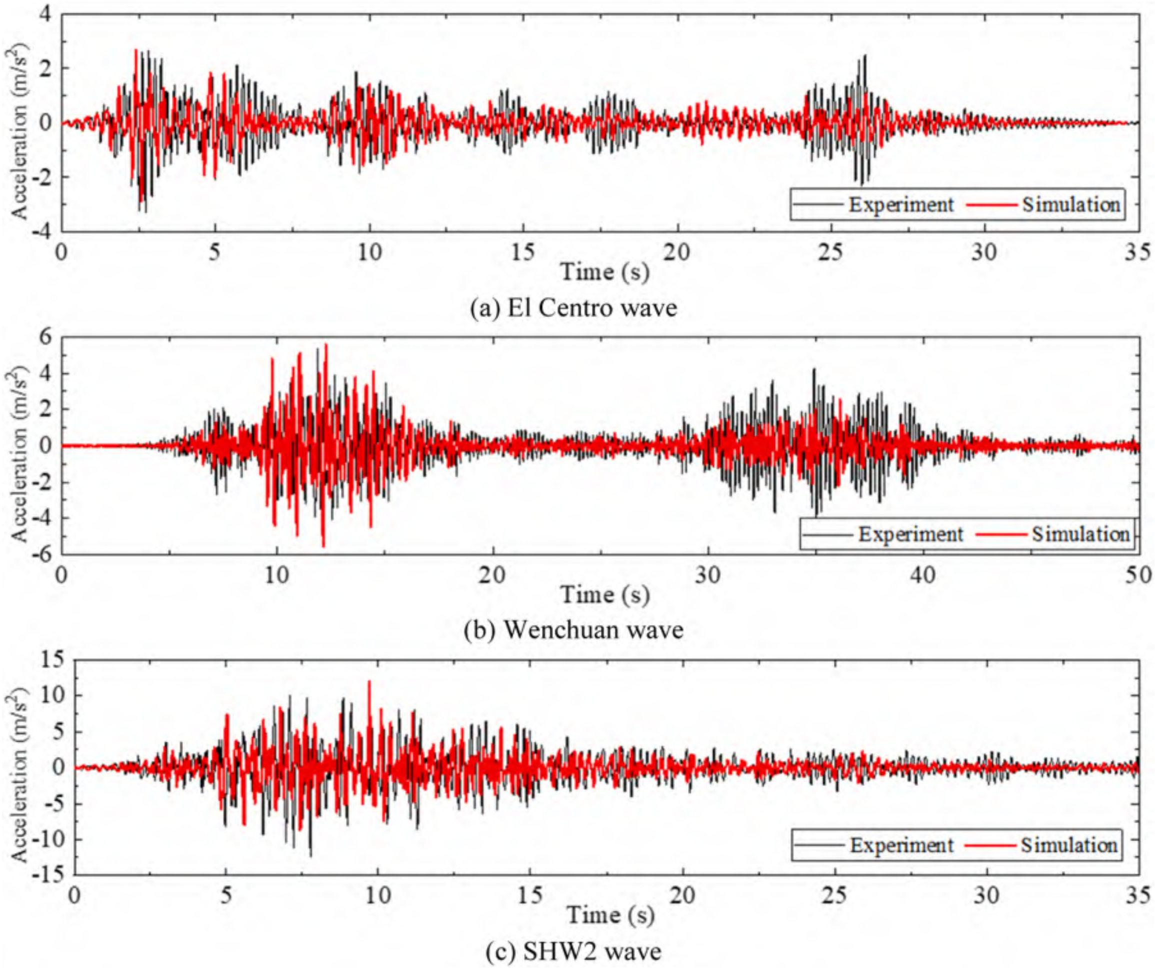

Fig. 22. Time-history curve of the roof acceleration.

Table 9
Comparison of inter-story displacement.

Excitation	Floor number	Inter-story displacement (mm)			
		Tested specimen	FE model	Error	Average error
El Centro	1	1.56	1.65	5.78 %	16.07 %
	2	1.28	1.58	23.50 %	
	3	1.31	1.55	18.92 %	
Wenchuan	1	3.27	3.54	8.25 %	12.01 %
	2	2.66	2.87	7.62 %	
	3	1.98	2.38	20.16 %	
SHW2	1	7.58	8.13	7.27 %	14.48 %
	2	6.98	7.82	12.03 %	
	3	5.51	6.84	24.13 %	

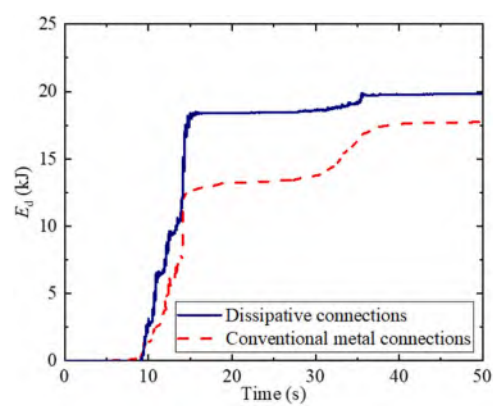

Fig. 23. Comparison of the total cumulative hysteretic energy consumption.

of the SRD-ABs and SRD-HDs was generally larger than that of the conventional metal ones throughout the entire earthquake process, with the final total energy dissipation being approximately 1.2 times that of the conventional metal connections. This indicates that the dissipative connections have superior energy dissipation capabilities.

(2) Regarding failure modes, damage in CLT structures with SRD-ABs and SRD-HDs mainly occurred in the yielding and fracture of the soft-steel ribs and the shear deformation of the rubber, while no significant damage was observed in the screws or the CLT panels, as shown in Fig. 9. This suggests that after earthquakes, the CLT structure can be easily repaired by simply replacing the dissipative connections, making the repair process straightforward and rapid. In contrast, for the CLT structures with conventional metal angle brackets and hold-downs, these connections may suffer from various failure modes, including embedment failure, local buckling or fracture of the metal plates, torsion of the metal plates, and pull-out of screws, as shown in Fig. 24, making repairs more difficult.

(3) In terms of seismic resilience, as seen from the load-displacement time-history curves of the typical angle bracket in Fig. 25, the conventional metal angle brackets underwent significant residual deformation (which could potentially indicate failure). In contrast, the dissipative ones exhibited much smaller residual deformations under the earthquakes, especially those with long durations like the Wenchuan wave,

(a) Embedment failure[41] (b) Fracture of metal plate[42] (c) Pull-out of screws[43]

Fig. 24. Typical failure modes in conventional metal hold-downs and angle brackets [41-43].

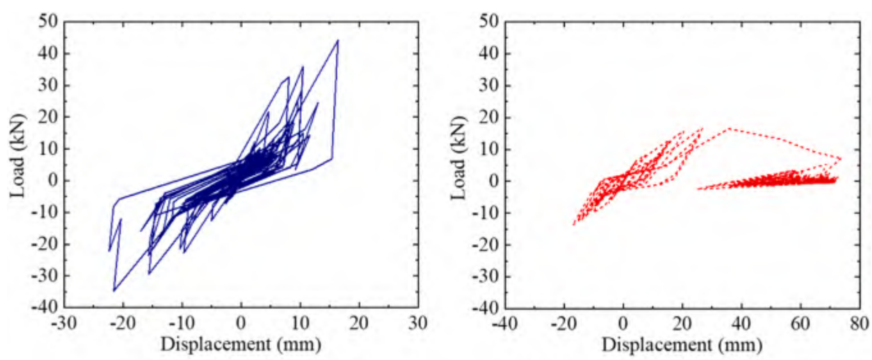

(a) Dissipative connection (b) Conventional metal connection

Fig. 25. Comparison of time-history load-displacement curves.

indicating superior seismic resilience. However, it should be mentioned that the comparative results presented in this section are primarily based on the FE models established in this study. With reasonable design, the CLT structures with conventional metal connections can also exhibit good seismic performance.

6. Conclusions

A series of full-scale shaking table tests on the CLT structures adopting dissipative angle brackets and hold-downs with soft-steel and rubber were performed. The dynamic properties of the tested specimens were determined, and the seismic responses were analyzed. Additionally, the tested full-scale specimen was duplicated numerically in OpenSees. Based on the experimental and numerical analysis, the main conclusions can be summarized as follows:

(1) The fundamental frequencies of Specimen I and II are 4.125 Hz and 3.625 Hz, respectively, with corresponding damping ratios of 3 % and 10 %. After the tests, their fundamental frequencies decreased to 3.875 Hz and 3.000 Hz, respectively, and the corresponding damping ratios increased to 5 % and 13 %.
(2) The mode shapes of Specimen I and II did not show significant changes before the tests with a PGA of 0.51 g, and their fundamental frequency only decreased by about 5 %. Meanwhile, the maximum inter-story displacement was approximately linearly correlated with the seismic intensity. These indicate that the specimens were in the elastic stage or only suffered minor damage, thanks to the great energy-dissipating capacity of the SRD-ABs and SRD-HDs.
(3) The acceleration amplification factors of the specimens exhibited an inverted triangle distribution from bottom to top. The average acceleration amplification factor of Specimen I is in the range of 1.3 to 4.2, while that of Specimen II varies from 1.2 to 2.8.
(4) The damage to the specimens mainly occurred at the SRD-ABs and SRD-HDs. For Specimen I, after tests with a PGA of 0.62, its damage mainly exhibited as the relative displacement at the dissipative ribs at SRD-HDs. For Specimen II, after tests with a PGA of 0.80 g, its damage was mainly exhibited as the yielding failure at the dissipative ribs. Nevertheless, no rubber debonding or CLT crush failure was observed, and the residual deformation of the specimen was small.
(5) Due to the removal of the CLT wall panels, the lateral stiffness of Specimen II decreased significantly compared with Specimen I. However, after tests with PGA of up to 0.80 g, the maximum inter-story drift of Specimen II was 1/60, and the damage mainly occurred at the SRD-ABs and SRD-HDs, indicating that the structures have achieved the performance objective of replaceability of dissipative connections and repairability of structures under the 9-degree rare earthquakes.
(6) Non-linear numerical models were developed to duplicate the seismic behavior of the CLT structures with novel dissipative connections. Satisfactory agreement between the test results and model predictions was observed in terms of dynamic properties, floor acceleration responses, and inter-story displacement responses.

CRediT authorship contribution statement

Haibei Xiong: Supervision, Project administration, Methodology, Funding acquisition, Conceptualization. **Tomoki Furuta:** Resources, Methodology, Conceptualization. **Yingda Zheng:** Visualization, Validation, Methodology, Investigation, Formal analysis, Data curation. **Zhe Wu:** Investigation, Data curation. **Jiawei Chen:** Writing – original draft, Methodology, Investigation, Formal analysis, Conceptualization.

Declaration of Competing Interest

The authors declare that they have no known competing financial interests or personal relationships that could have appeared to influence the work reported in this paper.

Data availability

Data will be made available on request.

Acknowledgements

This paper is funded by the National Natural Science Foundation of China (52308259, 51978502), the International Joint Research Laboratory of Earthquake Engineering (TMGFXK-2015-002-2), and the High-level Scientific Research Foundation of Nanjing Forestry University (2023020). The financial support is greatly appreciated.

References

[1] Brandner R, Flatscher G, Ringhofer A, Schickhofer G, Thiel A. Cross laminated timber (CLT): overview and development. Eur J Wood Wood Prod 2016;74:331–51.
[2] Li H, Wei Y, Yan L, Semple KE, Dai C. Structural behavior of steel dowel-reinforced cross-laminated bamboo and timber beams. Compos Struct 2023;318:117111.
[3] Sun X, He M, Li Z, Lam F. Seismic performance assessment of conventional CLT shear wall structures and post-tensioned CLT shear wall structures. Eng Struct 2019;196:109285.
[4] Li H, Wang BJ, Wei P, Wang L. Cross-laminated timber (CLT) in China: a state-of-the-art. J Bioresour Bioprod 2019;4:22–31.
[5] Popovski M, Gavric I. Performance of a 2-story CLT house subjected to lateral loads. J Struct Eng 2016;142:E4015006.
[6] Reynolds T, Foster R, Bregulla J, Chang W, Harris R, Ramage M. Lateral-load resistance of cross-laminated timber shear walls. J Struct Eng 2017;143:06017006.
[7] Hristovski V, Dujic B, Stojmanovska M, Mircevska V. Full-scale shaking-table tests of XLam panel systems and numerical verification: specimen 1. J Struct Eng 2013;139:2010–8.
[8] Ceccotti A, Sandhaas C, Okabe M, Yasumura M, Minowa C, Kawai N. SOFIE project–3D shaking table test on a seven-storey full-scale cross-laminated timber building. Earthq Eng Struct Dyn 2013;42:2003–21.
[9] Rinaldin G, Fragiacomo M. Non-linear simulation of shaking-table tests on 3-and 7-storey X-Lam timber buildings. Eng Struct 2016;113:133–48.
[10] van de Lindt JW, Furley J, Amini MO, Pei S, Tamagnone G, Barbosa AR, et al. Experimental seismic behavior of a two-story CLT platform building. Eng Struct 2019;183:408–22.
[11] Izzi M, Casagrande D, Bezzi S, Pasca D, Follesa M, Tomasi R. Seismic behaviour of Cross-Laminated Timber structures: a state-of-the-art review. Eng Struct 2018;170:42–52.
[12] Kržan M, Azinović B. Cyclic response of insulated steel angle brackets used for cross-laminated timber connections. Eur J Wood Wood Prod 2021;79:691–705.
[13] Liu J, Lam F. Experimental test of coupling effect on CLT angle bracket connections. Eng Struct 2018;171:862–73.
[14] Daneshvar H, Niederwestberg J, Letarte JP, Chui Y. Yield mechanisms of base shear connections for cross-laminated timber shear walls. Constr Build Mater 2022;335:127498.
[15] Trutalli D, Marchi L, Scotta R, Pozza L. Capacity design of traditional and innovative ductile connections for earthquake-resistant CLT structures. Bull Earthq Eng 2019;17:2115–36.
[16] Pei S, Popovski M, van de Lindt JW. Analytical study on seismic force modification factors for cross-laminated timber buildings. Can J Civ Eng 2013;40:887–96.
[17] Ringhofer A, Brandner R, Blaß HJ. Cross laminated timber (CLT): design approaches for dowel-type fasteners and connections. Eng Struct 2018;171:849–61.
[18] Bhandari S, Riggio M, Jahedi S, Fischer EC, Muszynski L, Luo Z. A review of modular cross laminated timber construction: implications for temporary housing in seismic areas. J Build Eng 2022:105485.
[19] AlNajjar A, Dodoo A. Modular multi-storey construction with cross-laminated timber: life cycle environmental implications. Wood Mater Sci Eng 2023;18:525–39.
[20] Tulonen L, Karjalainen M, Ilgin HE. Tall wooden residential buildings in Finland: what are the key factors for design and implementation? Eng Wood Prod Constr 2021.
[21] Chen J, Xiong H, Ventura CE. Non-linear simplified models for seismic response estimation of a novel tall timber-concrete hybrid structural system. Eng Struct 2021;229:111635.
[22] Chen J, Xiong H, Ventura CE. Seismic reliability evaluation of a tall concrete-timber hybrid structural system. Struct Des Tall Spec Build 2022:e1933.
[23] Scotta R, Marchi L, Trutalli D, Pozza L. A dissipative connector for CLT buildings: concept, design and testing. Materials 2016;9:139.
[24] Marchi L, Trutalli D, Scotta R, Pozza L. Macro-element modelling of a dissipative connection for CLT structures. Structures 2020;26:582–600.
[25] Wrzesniak D, Rodgers GW, Fragiacomo M, Chase JG. Experimental testing of damage-resistant rocking glulam walls with lead extrusion dampers. Constr Build Mater 2016;102:1145–53.
[26] D'Arenzo G, Casagrande D, Polastri A, Fossetti M, Fragiacomo M, Seim W. CLT shear walls anchored with shear-tension angle brackets: experimental tests and finite-element modeling. J Struct Eng 2021;147:04021089.
[27] Polastri A, Giongo I, Piazza M. An innovative connection system for cross-laminated timber structures. Struct Eng Int 2017;27:502–11.
[28] Hashemi A, Zarnani P, Masoudnia R, Quenneville P. Experimental testing of rocking cross-laminated timber walls with resilient slip friction joints. J Struct Eng 2018;144:04017180.
[29] Kramer A, Barbosa AR, Sinha A. Performance of steel energy dissipators connected to cross-laminated timber wall panels subjected to tension and cyclic loading. J Struct Eng 2016;142:E4015013.
[30] Chen J, Xiong H, Furuta T, Lu Y, Abbas N. Experimental and analytical studies on mechanical performance of innovative energy-dissipating hold-down for CLT structures. Constr Build Mater 2022;317:125966.
[31] Chen L, Xiong H, Li X, Lu Y, Kong Q. An ensemble learning approach to condition assessment of dissipative CLT connections based on piezoceramic sensor data. Eng Appl Artif Intell 2023;117:105514.
[32] Chen J, Peng Z, Furuta T, Xiong H. Mechanical properties and analytical model of a novel dissipative angle bracket for CLT structures. Eng Struct 2024;300:117229.
[33] Ministry of Housing and Urban-Rural Development of the People's Republic of China. Code for fire protection design of buildings, GB50016–2014. Beijing, China: China Architecture & Building Press; 2018.
[34] Ministry of Housing and Urban-Rural Development of the People's Republic of China. Code for seismic design of buildings, GB50011–2010. Beijing, China: China Architecture & Building Press; 2016.
[35] Ceccotti A. New technologies for construction of medium-rise buildings in seismic regions: the XLAM case. Struct Eng Int 2008;18:156–65.
[36] Casagrande D, Doudak G, Polastri A. A proposal for the capacity-design at wall-and building-level in light-frame and cross-laminated timber buildings. Bull Earthq Eng 2019;17:3139–67.
[37] Jing W, Renjie L, Chunlin W, Zhen Z. A modified capacity spectrum method with direct calculation of seismic intensity of points on capacity curve. J Earthq Eng 2011;15:664–83.
[38] Gagnon S, Pirvu C. Pointe-Claire. CLT handbook: cross-laminated timber. QC, Canada: FPInnovations; 2013.
[39] Gavric I, Fragiacomo M, Ceccotti A. Cyclic behavior of typical screwed connections for cross-laminated (CLT) structures. Eur J Wood Wood Prod 2015;73:179–91.
[40] Sun X, He M, Li Z, Shu Z. Performance evaluation of multi-storey cross-laminated timber structures under different earthquake hazard levels. J Wood Sci 2018;64:23–39.
[41] Cao J, Xiong H, Zhang F, Chen L, Cazador CR. Bayesian model selection for the nonlinear hysteretic model of CLT connections. Eng Struct 2020;223:111118.
[42] Chen J, Wang R, Furuta T, Xiong H. Experimental research on lateral performance of CLT shear walls with novel dissipative angle brackets and hold-downs. J Build Eng 2024:108929.
[43] Popovski M, Schneider J, Schweinsteiger M. Lateral load resistance of cross-laminated wood panels. In: Proceedings of the world conf. timber eng, 2010. Trentino, Italy: WCTE; 2010. p. 20–4.